



Structure and mechanical properties of novel lightweight refractory high entropy alloys NbMoTiZr-(Al/V): A combined first principles and experimental study

Wenjie Chen, Xinmei Li*

School of Mechanical Engineering, Xinjiang University, Urumchi 830017, China

ARTICLE INFO

Keywords:

Refractory high-entropy alloy
First-principle calculation
Phase structure
Elastic properties
Electronic structure

ABSTRACT

NbMoTaW refractory high entropy alloy (RHEA) has excellent high temperature mechanical properties, but low room temperature ductility and high density severely limit its practical applications. In the present work, to overcome this deficiency, the composition was adjusted, and the mechanical properties of four novel as-cast NbMoTiZr-(Al/V) lightweight refractory high entropy alloys (LRHEAs) were investigated by theoretical calculations combined with experimental methods. The first-principle calculations approach based on density functional theory predicts the mechanical properties of LRHEAs and explains the alloying effects at the atomic and electronic levels. The body-centered-cubic (BCC) phase structure of the alloys were predicted on the formation enthalpy and cohesive energy, as well as empirical parameters such as ΔS_{mix} , ΔH_{mix} , VEC, and the atomic size difference, in conjunction with CALPHAD and XRD. The microstructure of the LRHEAs were also analyzed by SEM. The experimental results, along with the calculated elastic constants and moduli, show significant improvement in the strength and ductility of NbMoTiZr-(Al/V) LRHEAs compared to NbMoTaW RHEA. LRHEAs exhibit elastic anisotropy and are therefore more suitable for use in engineering applications. The strengthening mechanisms of the alloys were analyzed in terms of total and partial densities of states, overlapping Mulliken population, charge density contour and atomic distances. The increased plasticity of LRHEAs is mainly due to the formation of Ti-Ti, Zr-Zr and Zr-Al metallic bonds in the alloys. The calculated results agree with the experimental results, indicating that first-principles calculations are an effective method for predicting the improved properties of lightweight refractory high-entropy alloys. The present work provides a good guideline for the design and research of lightweight refractory high entropy alloys.

1. Introduction

Compared to conventional alloys, high-entropy alloys have unique properties, such as the thermodynamic high-entropy effect[1], the severe lattice distortion effect[2], the slow diffusion effect[3], and the cocktail effect[4], which result in their microstructural manifestation in the form of face-centered-cubic (FCC), body-centered-cubic (BCC), or densely-arranged-hexagonal (HCP) structures rather than in the form of simple intermetallic compounds. These properties give high entropy alloys high hardness, strong oxidation resistance, outstanding mechanical properties, excellent wear resistance and corrosion resistance[5–9]. In 2010, Senkov et al.[10] first proposed a new type of RHEAs composed mainly of refractory metals (such as Nb, Ta, Mo, W, V, Zr and other elements). RHEAs with a high melting point, specific strength, high

temperature performance and mechanical properties are excellent, and are highly promising high temperature materials for aerospace, petrochemical and other engineering applications. In particular, the MoNbTaW RHEA has a yield strength of over 400 MPa at 1600 °C, with excellent high temperature stability and retention of a single BCC structure[11]. The yield strength of Inconel 718 nickel-based high temperature alloy at 1000 °C is only 200 MPa. Therefore, NbMoTaW RHEA is currently a hot spot in the research field of refractory high entropy alloys. However, the higher density (13.75 g/cm³) and lower room temperature ductility (fracture strain of only 2.6%) of NbMoTaW RHEA has severely limited its further development and engineering applications in fields such as aerospace.

Several studies in recent years have shown that the addition of moderate amounts of Zr can improve the strength and hardness of alloys

* Corresponding author.

E-mail address: lxxmj2009@126.com (X. Li).



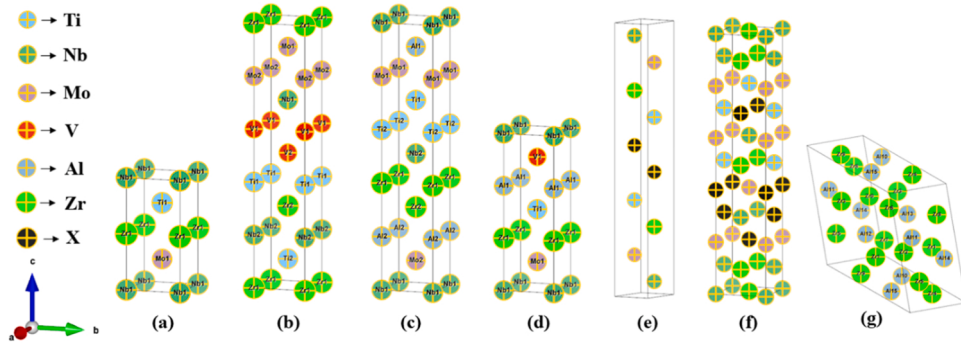


Fig. 1. NbMoTiZr-(Al/V) LRHEAs SQS and Zr₅Al₃ supercell model after structural relaxation. BCC: (a) NbMoTiZr 1×1×2 (b) NbMoTiZrV 1×1×5 (c) NbMoTiZrAl 1×1×5 (d) NbMoTiZrAlV 1×1×3 (e) HCP 1×1×5 (f) FCC 1×1×5 (g) Zr₅Al₃ 1×1×2.

[12,13], while the addition of Al and Ti can significantly reduce the density of alloys and improve the high temperature performance of alloys[14–18]. For example, Yurchenko et al.[19] investigated the microstructure and mechanical properties of AlNbTiVZr_x ($x = 0\text{--}1.5$) and found that the strength of AlNbTiVZr_x alloys change significantly with increasing Zr content, with the room temperature compressive yield strength increasing from 1000 MPa to 1535 MPa, and the plasticity of the alloys increasing from 6% to over 50%. Vipul et al.[20] showed that the addition of Al to Al_xTiZrNbHf RHEAs improved the mechanical properties and wear resistance of the alloys due to second phase strengthening and severe lattice distortion. Therefore, the addition of Al element can significantly change the crystal structure, microstructure morphology and mechanical properties. Han et al.[21] investigated the effect of Ti element on NbMoTaW and VNbMoTaW and found that the addition of Ti element is beneficial to improve the strength and compression plasticity of RHEAs at room temperature. Salishchev et al. [22] found that the addition of V significantly increased the hardness of CoCrFeNi-based high entropy alloys from 160 Hv to 524 Hv and the compressive yield strength to $\sigma_{0.2} = 1435$ MPa. Zhao et al.[23] reported that by replacing the W element in MoNbTaW with the V element, the MoNbTaV alloy still has a single body-centered-cubic structure, with a high yield stress of 1.5 GPa and a compressive fracture strain of 21% at room temperature, which is significantly higher than those of MoNbTaW, and its theoretical density is reduced to 10.69 g/cm³. Chen et al. [24] reported that by substituting expensive and refractory Ta and W elements with Ti and V elements, MoNbTiV alloys with equal atomic ratios were produced with an as-cast compressive yield strength of 1200 MPa at room temperature, a compressive strain elongation at fracture of up to 25.62%, and a hardness of 440.7 HV, with a theoretical density further reduced to 7.32 g/cm³. Therefore, adjusting the elements of the alloying system can effectively reduce the density and improve the mechanical properties of RHEAs. In this study, based on Nb-Mo-Ta-W by adjusting the alloying system, Ta and W elements with poor plasticity and high density were replaced by Ti, Zr, Al and V. Four novel NbMoTiZr-(Al/V) LRHEAs were designed and prepared to analyze the microstructure of the alloys and their mechanical properties.

Most of the current research on RHEA has focused on experimental studies, with fewer theoretical calculations on the mechanical strengthening of alloys, especially the lack of further exploration and explanation of the mechanism from the atomic and electronic (e.g., electronic structure, energy band structure, and charge density) perspectives. Therefore the mechanical properties, phase structure, lattice constants, density and elastic properties of NbMoTiZr-(Al/V) LRHEAs were investigated by first-principle calculations. The energy bands, density of states, and charge density of NbMoTiZr-(Al/V) alloys were calculated to investigate the mechanism of strength and ductility of NbMoTiZr-(Al/V) alloys.

2. Methods

2.1. Theoretical methods and calculation models

The crystal structures of the NbMoTiZr-(Al/V) alloys and the Zr₅Al₃ intermetallic compound were shown in Fig. 1. NbMoTiZr-(Al/V) alloys crystals were automatically generated using the CASTEP module[25] and special quasirandom structure (SQS)[26] in conjunction with the "mcsqs" code from the Alloy Theory Automation Toolkit (ATAT)[27] to ensure the short-range disorder properties of high-entropy alloys. The calculations use the Generalised Gradient Approximation (GGA)[28] and Perdew Burke Ernzerhof (PBE)[29] generalizations to describe the electron-exchange correlation interactions. The Norm Conserving Pseudopotential (NCP)[30] represents the electron-ion interrelationships, and the BFGS algorithm is used to solve the Schrödinger equation [31]. During the structural optimization process, the crystal structure and atoms were sufficiently relaxed until the SCF iterative convergence conditions were reached: The total energy $< 1 \times 10^{-5}$ eV/atom; maximum force < 0.03 eV/ Å; maximum stress < 0.05 GPa; maximum displacement < 0.001 Å. After the convergence tests, the energy cutoff of the NbMoTiZr-(Al/V) LRHEAs were set to 480 eV, and the K-points were set to 8×8×2.

2.2. Experimental

To verify the theoretical results, the as-cast NbMoTiZr-(Al/V) LRHEAs with a purity of 99.9% were produced in a WK-II non-self-consuming vacuum arc furnace. Due to the presence of refractory metal elements, the alloys had to be rotated and melted at least 7 times, with the alloys being rotated before each remelting. In addition, the melt was kept in a liquid state for 10 min during each melting process to ensure homogeneous composition and organization. The as-cast were approximately 20 mm in diameter and 10 mm in height. The phase structures of the NbMoTiZr-(Al/V) LRHEAs were characterized by D&Advance X-ray diffraction (XRD, Cu K α radiation) with the scanning range from 20°–20°–90°, and the scanning speed of 5°/min. The microstructure and morphology were characterized using Super 55VP and SYMMETRY emission scanning electron microscopy (SEM) with electron backscattering diffractometry (EBSD). The hardness was tested using a TMHV-1000Z microhardness instrument with an indenter load of 100 g and a loading time of 15 s, by averaging the hardness values at 15 arbitrary points as the microhardness value of the alloy. The density of the alloys were measured by hydrostatic weighing, and four samples were averaged after three separate measurements in the same state to minimize experimental and manual errors. The compression performance of the alloys were tested using an ETM105D universal testing machine, with a compression sample size of Φ4mm × 6 mm. The surface of the compression test samples were lightly polished to reduce the friction coefficient between the sample and the specimen machine, and the

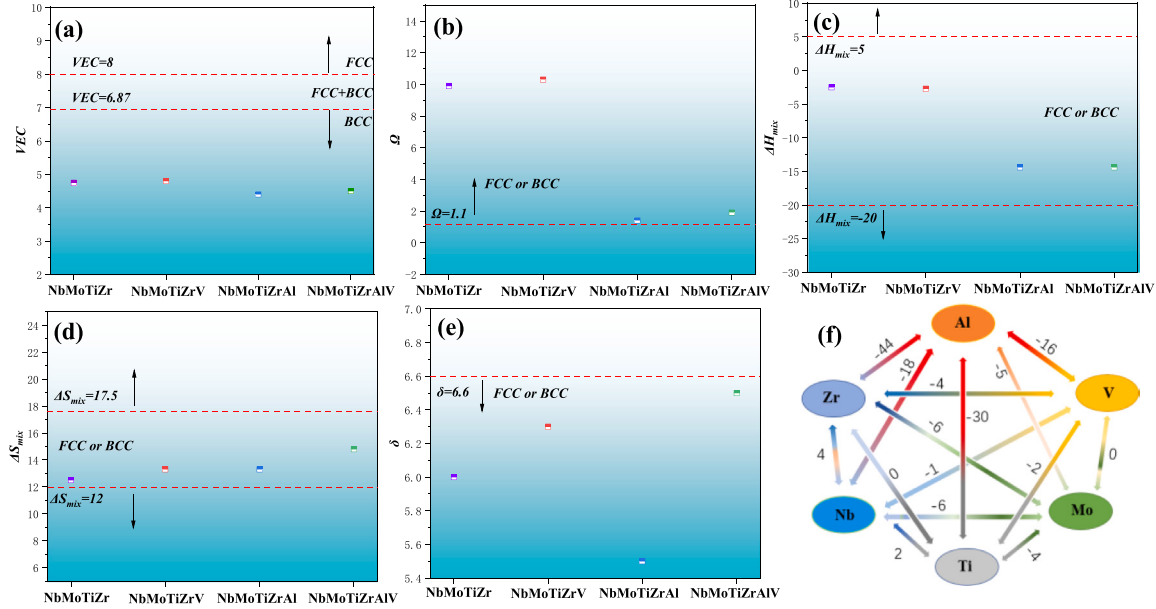


Fig. 2. VEC, Ω , ΔH_{mix} , ΔS_{mix} , δ and Binary mixing enthalpy of NbMoTiZr-(Al/V) LRHEAs.

compression test loading rate was 0.5 mm/min.

2.3. Elastic constants and polycrystalline elastic modulus

The elastic constants (C_{11} , C_{12} , C_{44}) and elastic moduli (bulk modulus B , shear modulus G , Young's modulus E and Poisson's ratio ν) can reflect the key performance parameters of the mechanical properties of crystalline materials. Typically, elastic constants and elastic moduli were positively correlated. In this work, the Voigt-Reuss-Hill (VRH) approximation method[32] was used to calculate the single crystal elastic constants C_{11} , C_{12} and C_{44} for the NbMoTiZr-(Al/V) LRHEAs SQS supercell structures and to calculate and derive their polycrystalline elastic moduli B , G , E and ν . They are calculated by the following equations:

$$B = \frac{1}{3}(C_{11} + 2C_{12}) \quad (1)$$

$$G = \frac{1}{2}(G_V + G_R) \quad (2)$$

$$G_V = \frac{1}{5}(C_{11} - C_{12} + 3C_{44}) \quad (3)$$

$$G_R = \frac{5(C_{11} - C_{12})C_{44}}{4C_{44} + 3(C_{11} - C_{12})} \quad (4)$$

$$E = \frac{9BG}{3B + G} \quad (5)$$

$$\nu = \frac{3B - 2G}{2(3B + G)} \quad (6)$$

In the above equation, G_V and G_R are the values obtained by Voigt's and Reuss's methods respectively, while G is the average of the Hill's method. In general, Voigt's method overestimates the modulus of elasticity and Reuss's method underestimates the modulus of elasticity.

In addition, the values of the elastic constants were used to determine the mechanical stability of the crystal structure, the elastic anisotropy ratio A_{VR} and the bonding properties of the alloy system. For cubic crystal structures, the elastic stability[33] can be determined by Eq. (7).

$$C_{11} > 0; C_{44} > 0; (C_{11} - C_{12}) > 0; C_{11} + 2C_{12} > 0 \quad (7)$$

Elastic anisotropy has an important influence on the microcracking and deformation of materials. In this paper, the elastic anisotropy of four NbMoTiZr-(Al/V) LRHEAs is predicted by Eq. (8). The reference value $A_{VR}=0$ indicates that the material is completely isotropic, $A_{VR}=1$ indicates that the material is completely anisotropic, and in between indicates the degree of anisotropy[34].

$$A_{VR} = \frac{G_V - G_R}{G_V + G_R} \quad (8)$$

Cauchy pressure ($C_{12} - C_{44}$) predicts whether the alloy forms a metallic bond or not, and is an important parameter that can predict the bonding characteristics and intrinsic plasticity of the material. Cauchy pressure ($C_{12} - C_{44}$) > 0 indicates that the crystal is ductile metallically bonded[35]. Cauchy pressure of the four NbMoTiZr-(Al/V) LRHEAs are judged by Eq. (9).

$$(C_{12} - C_{44}) > 0 \quad (9)$$

3. Results and discussion

3.1. Phase structure

HEAs have usually been reported to form FCC, BCC, or HCP solid solution structures. However, a considerable proportion of High-Entropy Alloys (HEAs) comprise not only a solitary disordered solid solution phase but also feature nanophases, amorphous phases, and intermetallic compound phases. The phase composition in HEAs has a crucial influence on their performance and thus on their range of applications. The average valence electron concentration VEC, mixture entropy (ΔS_{mix}), mixture enthalpy (ΔH_{mix}), the atomic size difference δ and the composite parameter Ω [36,37] are generally used to predict the phase structure of high entropy alloys as in Eq. (10)-(14). Therefore, this study presents a theoretical computational analysis of the phase formation of NbMoTiZr-(Al/V) LRHEAs to provide modeling information for subsequent first-principles simulation analysis.

$$\Delta S_{\text{mix}} = -R \cdot \ln n \quad (10)$$

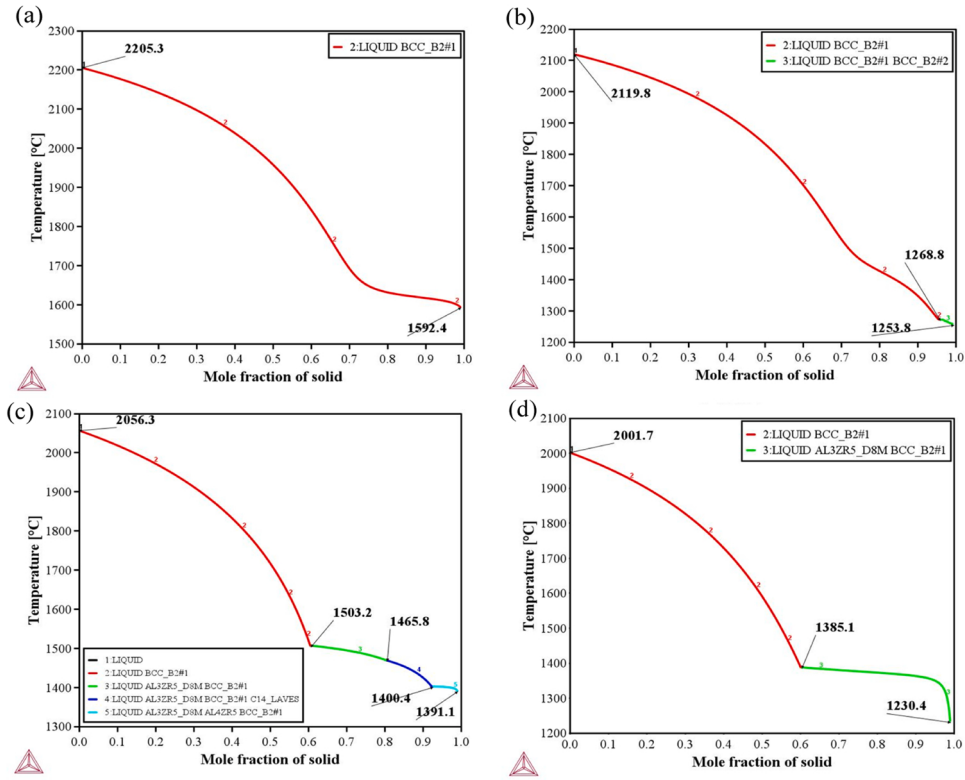


Fig. 3. Non-equilibrium solidification phase diagram of NbMoTiZr-(Al/V) LRHEAs: (a)NbMoTiZr (b) NbMoTiZrV (c) NbMoTiZrAl (d) NbMoTiZrAlV.

$$\Delta H_{\text{mix}} = \sum_{i=1, i \neq j}^n 4\Delta H_{ij}^{\text{mix}} c_i c_j \quad (11)$$

$$VEC = \sum_{i=1}^n c_i (VEC)_i \quad (12)$$

$$\bar{R} = \sqrt{\sum_{i=1}^n c_i (1 - r_i/\bar{r})^2}, \bar{r} = \sum_i^n c_i r_i \quad (13)$$

$$\Omega = \frac{T_m \Delta S_{\text{mix}}}{|\Delta H_{\text{mix}}|}, \quad T_m = \sum_{i=1}^n c_i (T_m)_i \quad (14)$$

Where R is gas constant, c_i , r_i , \bar{r} , $(VEC)_i$ and $(T_m)_i$ are the molar fraction, atomic radius, average atomic radius, valence electron concentration and melting point. The calculated empirical parameters and predicted phases are shown in Fig. 2. The values of the various

parameters of the NbMoTiZr-(Al/V) LRHEAs are within the numerical range of the formation of a disordered solid solution phase.

CALPHAD was used to further predict the phase structures of NbMoTiZr-(Al/V) LRHEAs. Due to the high cooling rate of arc melting, there is not enough time to reach equilibrium during solidification. Therefore, especially in RHEAs [38,39]. The results of equilibrium phase calculations are often in disagreement with experimental results. On the contrary, the solid phase that has solidified in the Scheil solidification simulation does not take into account reverse diffusion, and the Scheil solidification simulation can be regarded as a solidification with a very fast cooling rate. Fig. 3 shows the non-equilibrium solidification phase diagram of NbMoTiZr-(Al/V) LRHEAs calculated using the Scheil-Gulliver model. The phase diagram results for NbMoTiZr and NbMoTiZrV LRHEAs show that only a single BCC phase is formed during solidification of the alloys. For NbMoTiZrAl and NbMoTiZrAlV LRHEAs the phase diagram results after the addition of Al show that the BCC phase is formed first, and then the Zr₅Al₃ phase starts to form when the

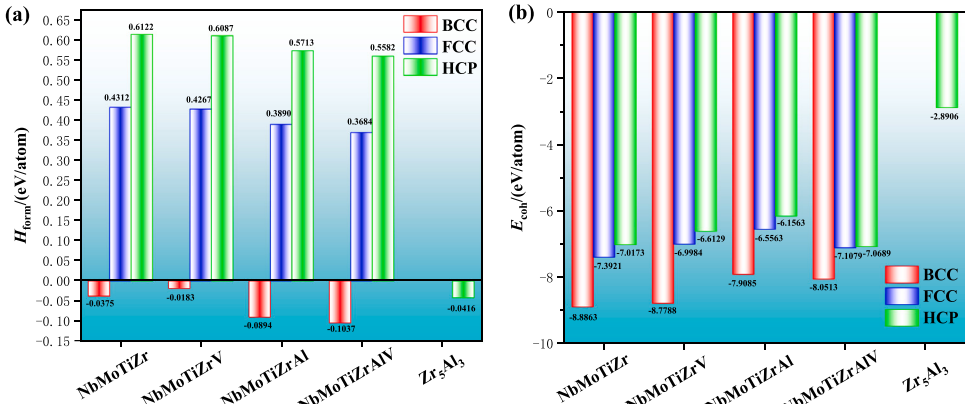


Fig. 4. The formation enthalpy (a) and cohesive energy (b) of NbMoTiZr-(Al/V) LRHEAs and Zr₅Al₃ intermetallic compound.

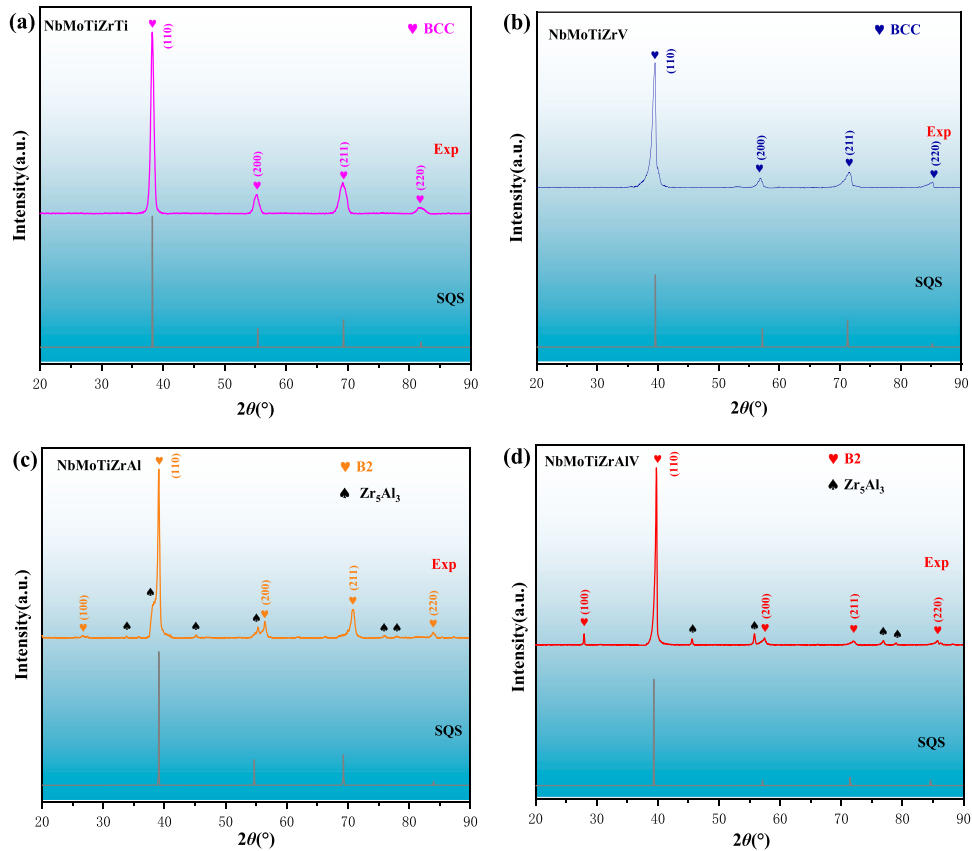


Fig. 5. Experimental and theoretical XRD patterns of NbMoTiZr-(Al/V) LRHEAs (a) NbMoTiZr (b) NbMoTiZrV (c) NbMoTiZrAl (d) NbMoTiZrAlV.

temperature is reduced to 1503.2 °C and 1385.1 °C, respectively, and finally to complete solidification.

In addition to the above empirical formulations and CALPHAD phase diagram simulations, predicting the thermodynamic stability and phase structure of high entropy alloys from an energetic point of view is also a commonly used method. The formation enthalpy (H_{form}) and cohesive energy (E_{coh}) are often used to characterize the thermodynamic stability of alloy systems [40,41]. Negative values of the formation enthalpy and larger absolute values indicate that this substance is more likely to form. The lower the cohesive energy, the easier it is for them to form thermodynamically stable structures. The formation enthalpy and cohesive energy of the BCC structure of NbMoTiZr-(Al/V) LRHEAs were calculated according to Eqs. (15) and (16).

$$H_{\text{form}} = \frac{1}{\sum_{i=1}^n x_i} \left(E_{\text{total}} - \sum_{i=1}^n x_i E_{\text{solid}}^{M_i} \right) \quad (15)$$

$$E_{\text{coh}} = \frac{1}{\sum_{i=1}^n x_i} \left(E_{\text{total}} - \sum_{i=1}^n x_i E_{\text{atom}}^{M_i} \right) \quad (16)$$

In Eqs. (15) and (16), E_{total} is the total energy of the optimized NbMoTiZr-(Al/V) LRHEAs SQS model, x_i is the number of atoms contained in the system by the alloying element M_i , $E_{\text{atom}}^{M_i}$ expresses the energy of a single M atom in the solid state. The energies of individual atomic structures have been calculated using the same parameter settings as for the optimization of the LRHEAs structures. As shown in Fig. 4 for NbMoTiZr-(Al/V) LRHEAs and Zr₅Al₃ intermetallic compound H_{form} and E_{coh} . The H_{form} of the four BCC structures of LRHEAs and HCP structures of Zr₅Al₃ intermetallic compound are all negative, indicating that they are all thermodynamically stable structures. While NbMoTiZrAl and NbMoTiZrAlV are more likely to form thermodynamically stable structures. In contrast, all four FCC and HCP structures are

positive, indicating that the BCC structure is superior to the other two structures in all alloys. For the cohesive energy it can be seen that the values of the four BCC structures of LRHEAs range from -7.9085 to -8.8863 eV/atom, whereas the Ni₃Al alloy phase has E_{coh} value of only -4.3036 eV/atom [42]. Compared to Ni₃Al alloys, more external work will be required to make the four LRHEAs structures decompose into individual atoms, indicating that the BCC structures of these four alloys have higher strength as well as greater structural stability.

Fig. 5 shows the experimental and theoretical XRD patterns of NbMoTiZr-(Al/V) LRHEAs. The experimental XRD patterns were analyzed and it can be seen from Fig. 5 that all four NbMoTiZr-(Al/V) LRHEAs are composed of BCC structures. Among them, NbMoTiZr and NbMoTiZrV alloys have a single BCC disordered solid solution structure; NbMoTiZrAl alloy consists of a B2 phase and a hexagonal Zr₅Al₃ phase, where the superlattice reflection peak of the (100) BCC is located at 27°, and the lattice parameter is $a_{\text{B2}} = 0.3194$ nm, indicating that the BCC is an ordered phase [43]. The NbMoTiZrAlV alloy is composed of both B2 and hexagonal Zr₅Al₃ phases as compared to the NbMoTiZrAl alloy, but there is a significant decrease in the Zr₅Al₃ phases due to a decrease in the relative Zr content. In addition, the intensity of the diffraction peaks of the Zr₅Al₃ phase is much smaller than that of the BCC phase, and the dominant phase in the alloy is still the BCC phase, which is probably due to the high entropy effect of the high entropy alloys hindering the formation of the Zr₅Al₃ phase. Theoretical XRD patterns were calculated by powder diffraction and the BCC phases were all correctly identified in the XRD patterns. The experimental results are in good agreement with the simulated data and also with the results of the CALPHAD phase diagram simulation calculations predicting the phase composition. Furthermore, the tendency of the strong peaks of NbMoTiZr-(Al/V) LRHEAs to shift to higher angles indicates that the lattice parameter decreases based on the incorporation of relatively small atomic sizes of V and Al atoms into the tetrameric NbMoTiZr LRHEA.

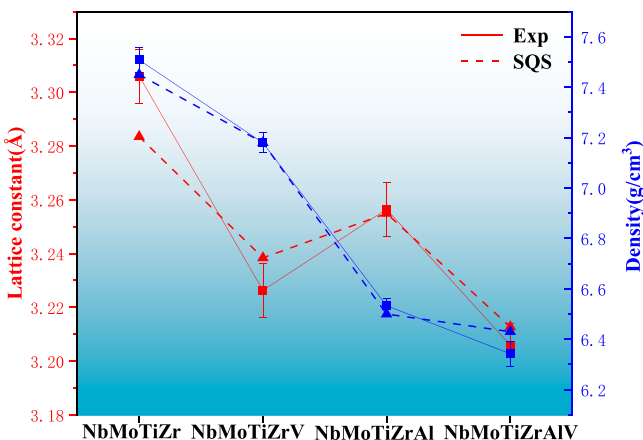


Fig. 6. Experimental and theoretical lattice constants and densities of NbMoTiZr-(Al/V) LRHEAs: (a) NbMoTiZr, (b) NbMoTiZrV, (c) NbMoTiZrAl, (d) NbMoTiZrAlV.

Fig. 6 shows the lattice constants and densities of NbMoTiZr-(Al/V) LRHEAs calculated by the SQS model and measured experimentally. It is clear that the addition of the elements V and Al reduces the lattice parameters of the alloy, a phenomenon that can be attributed to the

variations in the atomic sizes present. The decreasing trend of the calculated lattice constants is similar to the experimental data results with less error. The addition of V and Al elements reduces the lattice parameter of the alloy, a phenomenon that is attributed to the differences in atomic sizes present. Measurements of the alloy densities by hydrostatic weighing are in good agreement with the calculated densities of the four alloys. The above calculations show that the above parameters and models are reasonable and therefore the BCC NbMoTiZr-(Al/V) LRHEAs model is proposed to be used to calculate its elastic properties and electronic structure.

3.2. Microstructure

Fig. 7 shows the elemental planar distribution of the four LRHEAs. Typical dendritic organization can be observed in the microstructure of these four alloys, which is mainly due to the difference in the melting points of the constituent elements of the alloys, and the microstructures of the high entropy alloys produced by vacuum arc melting usually also show typical dendritic as well. It can be seen that the microstructure of the alloys were relatively dense and uniform, and only a small number of micropores were generated in the microstructure of the alloys. The dendritic and interdendritic regions in the microstructure of the four alloys were labeled by DR and IR. The distribution of several elements in the alloys in the dendritic and interdendritic regions is very unbalanced.

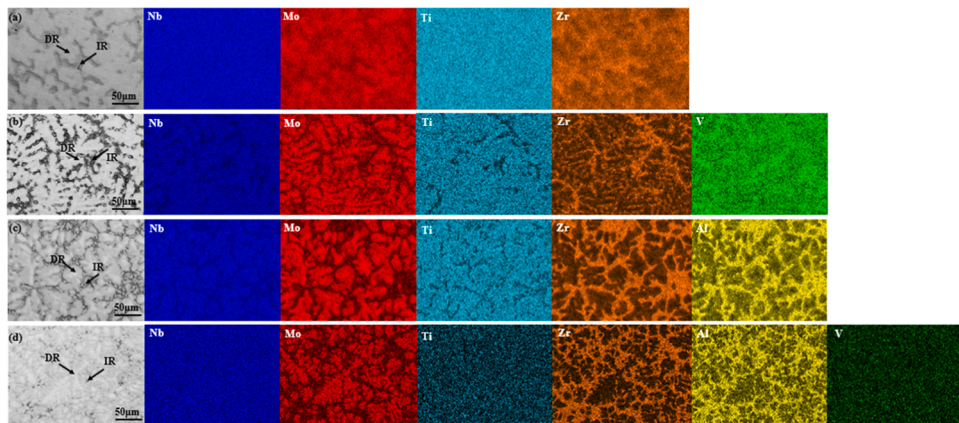


Fig. 7. BSE image of as-cast LRHEAs and corresponding mappings: (a) NbMoTiZr (b) NbMoTiZrV (c) NbMoTiZrAl (d) NbMoTiZrAlV.

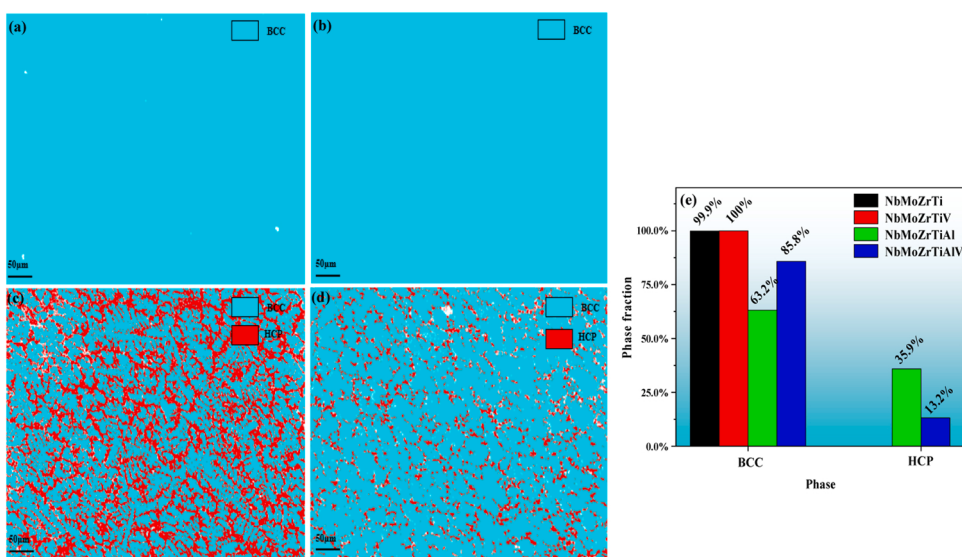


Fig. 8. Phase map of as-cast LRHEAs (a) NbMoTiZr (b) NbMoTiZrV (c) NbMoTiZrAl (d) NbMoTiZrAlV and (e) phase fraction.

Table 1

Nine independent elastic constants in the SQS supercell model of optimized NbMoTiZr-(Al/V) LRHEAs.

Alloys	C_{11}	C_{12}	C_{13}	C_{22}	C_{23}	C_{33}	C_{44}	C_{55}	C_{66}
NbMoTiZr	243	97	96	244	96	200	14	14	15
NbMoTiZrV	225	109	114	225	114	170	36	36	46
NbMoTiZrAl	181	114	111	180	110	150	52	52	75
NbMoTiZrAlV	190	148	105	190	105	168	39	39	63

Table 2

The mean elastic constants (C_{ij}/GPa), bulk modulus (B/GPa), shear modulus (G/GPa), Young's modulus (E/GPa), Poisson's ratio (ν) and Cauchy pressure ($C_{12}-C_{44}/\text{GPa}$) of NbMoTiZr-(Al/V) LRHEAs.

Alloys	C_{11}	C_{12}	C_{44}	B	G	E	B/G	ν	$C_{12}-C_{44}$	A_{VR}
NbMoTiZr	229	96	14	140	28	79	5	0.406	82	0.25
NbMoTiZrV	207	112	39	144	42	115	3.42	0.367	73	0.01
NbMoTiZrAl	170	111	60	131	45	121	2.91	0.346	52	0.06
NbMoTiZrAlV	183	119	47	140	40	110	3.5	0.369	72	0.02

Table 3

The lattice constants and elastic mechanical constants of the Zr_5Al_3 intermetallic compound.

Alloys	a	c	C_{11}	C_{12}	C_{13}	C_{33}	C_{44}	B	G	E	B/G	ν
Zr_5Al_3	8.3625	5.4871	200	68	52	151	37	98	51	131	1.92	0.278

From the mapping images, it can be seen that the high melting point elements Nb and Mo elements are enriched in DR, the low melting point Zr is enriched in IR, and the Ti element is almost evenly distributed in DR and IR. After the addition of the V element, the melting point of the V element is relatively low, so the proportion of V element polarization between dendrites is high. After the Al element is added, since the mixing enthalpy of Zr and Al elements is -44 kJ/mol , which is the minimum value in this alloy system, Zr and Al are more easily combined to form intermetallic compounds than other elements during solidification, therefore, so Zr and Al form a solution with other elements, and when solidification starts, Mo, Nb and Ti solidify first to form dendrites. Mo, Nb and Ti are less compatible with Zr, making the low melting point Zr-Al solution repulsive to the interdendritic crystals.

The alloys were non-equilibrium solidified in the experiments, so the results of the combined phase composition calculations are in good agreement with the XRD and CHALPHA analyses. The phase map in Fig. 8 shows that a single BCC phase is formed in both NbMoTiZr and NbMoTiZrV alloys. At the same time, BCC and HCP phases were formed in NbMoTiZrAl and NbMoTiZrAlV alloys. Fig. 8(e) shows the phase fractions of the four LRHEAs, with the highest HCP phase of 35.9% in the NbMoTiZrAl alloy. Combined XRD, SEM and EBSD analyses indicate that the HCP phase is a hexagonal Zr_5Al_3 intermetallic compound.

3.3. Elastic properties

Elastic properties describe the mechanical behavior of materials under strain, which is a common structural deformation in materials processing. As such, they contribute to the understanding of the response of material structures to stress, mechanical strength and phase transitions. It is essential to calculate the elastic constants of the four newly designed LRHEAs materials from first principles, which will help to provide a theoretical reference for practical preparation and analytical characterization. Referring to the averaging scheme proposed by Gao et al. [44] to obtain single crystals C_{11} , C_{12} and C_{44} with cubic structure, the elastic constant matrices of the four LRHEAs SQS supercellular structures were calculated by the CASTEP program. Their elastic constants C_{ij} and values of bulk modulus B, shear modulus G, Young's modulus E and Poisson's ratio ν were calculated. Table 1 and Table 2 show the calculated values of the above parameters for the four LRHEAs. Table 3 shows the lattice constants and elastic mechanical constants of the Zr_5Al_3 intermetallic compounds.

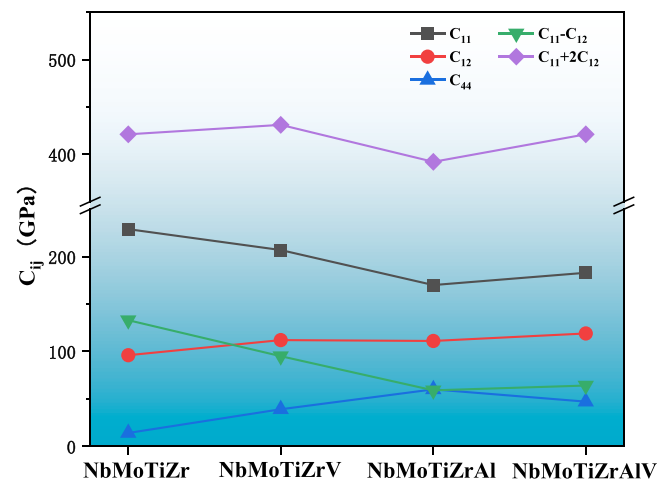


Fig. 9. C_{ij} values for NbMoTiZr-(Al/V) LRHEAs.

$$C_{11} = \frac{C_{11} + C_{22} + C_{33}}{3}, C_{12} = \frac{C_{12} + C_{23} + C_{13}}{3}, C_{44} = \frac{C_{44} + C_{55} + C_{66}}{3} \quad (17)$$

C_{11} , C_{12} and C_{33} denote the ability of the crystal structure to resist axial strain along the [001], [010] and [001] crystallographic directions respectively, while C_{44} , C_{55} and C_{66} denote their ability to resist shear deformation on the (100), (010) and (001) crystallographic planes. It can be seen that they are anisotropic in their ability to resist axial strain in the [001], [010] and [001] directions and in their ability to resist shear deformation at the grain planes (100), (010) and (001). The order of the resistance to axial deformation (C_{11}) of the four LRHEAs structures are: NbMoTiZr > NbMoTiZrV > NbMoTiZrAlV > NbMoTiZrAl and the order of shear deformation resistance (C_{44}) is NbMoTiZrAl > NbMoTiZrAlV > NbMoTiZrV > NbMoTiZr. C_{12} indicates the modulus of resistance to shear deformation along the [110] grain direction in the (110) grain plane, and its order of magnitude is: NbMoTiZrAlV > NbMoTiZrV > NbMoTiZrAl > NbMoTiZr. The body-centered-cubic crystal structure has three independent elastic constants, as shown in Fig. 9. In addition, the Born-Huang criterion shown in Eq. (7) is

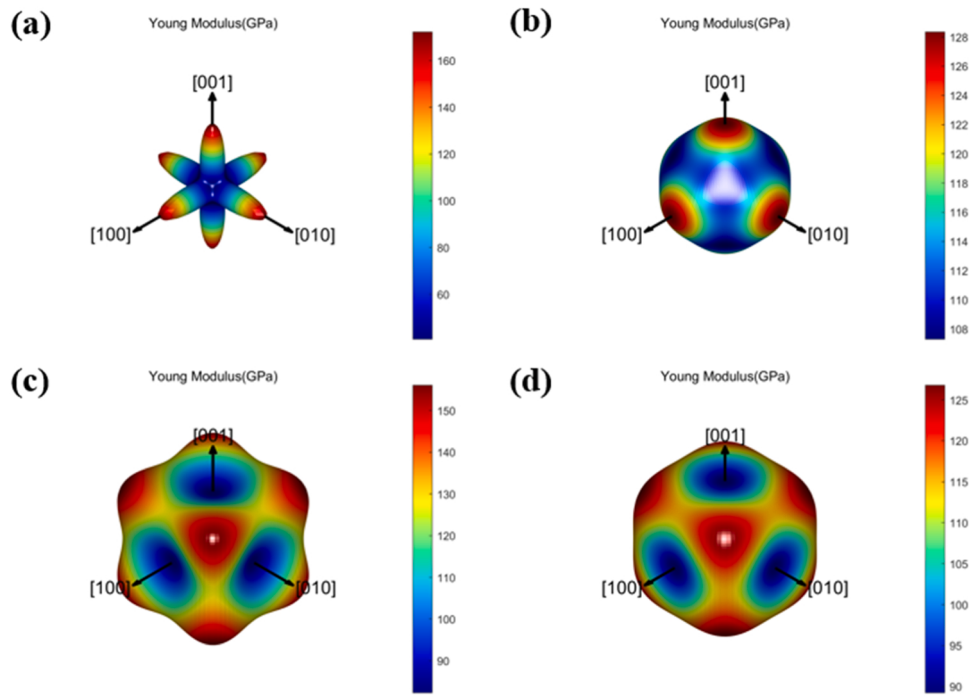


Fig. 10. 3D diagram of Young's modulus of NbMoTiZr-(Al/V) LRHEAs (a) NbMoTiZr (b) NbMoTiZrV (c) NbMoTiZrAl (d) NbMoTiZrAlV.

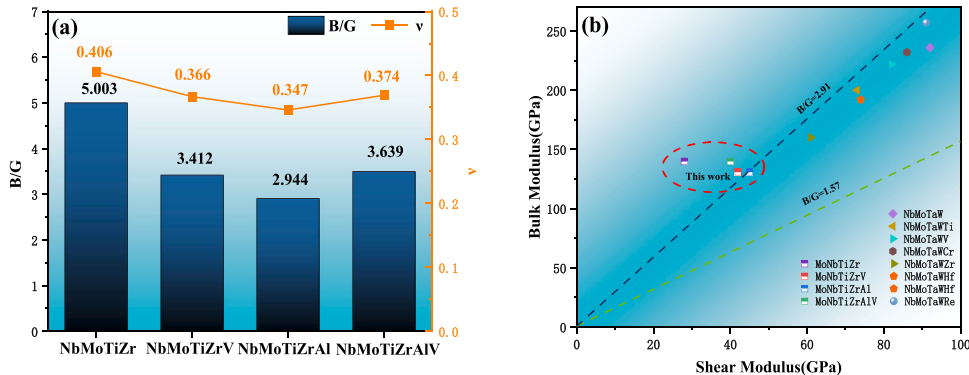


Fig. 11. B/G and ν of NbMoTiZr-(Al/V) LRHEAs and NbMoTaW-based RHEAs.

commonly used to predict the mechanical structural stability of high entropy alloys. From the calculation, it can be seen that their elastic stiffness constants C_{ij} satisfy the Born-Huang mechanical stability, indicating that the SQS structures of all four alloys are mechanically stable.

The A_{VR} of the four NbMoTiZr-(Al/V) LRHEAs were calculated and listed in Table 2. The calculated A_{VR} of the NbMoTiZr, NbMoTiZrV, NbMoTiZrAl, and NbMoTiZrAlV LRHEAs were 0.25, 0.01, 0.06, and 0.02, respectively. The elastic anisotropy of the four LRHEAs follows the following relationship: NbMoTiZr > NbMoTiZrAl > NbMoTiZrAlV > NbMoTiZrV. Young's modulus (E) can be seen as a reflection of how difficult it is for a material to deform elastically, the higher the Young's modulus the stiffer rigid the material is and the less likely it is to deform. The anisotropic nature of Young's modulus can lead to significant differences in material properties in different directions. The anisotropy of the calculated Young's modulus was predicted and the results of the 3D plot are shown in Fig. 10. It can be seen that the Young's moduli of the four NbMoTiZr-(Al/V) LRHEAs have different degrees of anisotropy and their elastic anisotropy follows the following relationship: NbMoTiZr > NbMoTiZrAl > NbMoTiZrAlV > NbMoTiZrV. The anisotropy predicted by the 3D Young's modulus were in agreement with the

anisotropy factor A_{VR} prediction.

In addition, the Pugh ratio (B/G), Poisson's ratio ν and the Cauchy pressure ($C_{12}-C_{44}$) can be used to predict the plasticity/brittleness of the alloy. $B/G = 1.57$, as a critical value, when $B/G > 1.57$, the material behaves as plastic, and the higher the B/G value, the better the plasticity, and when $B/G < 1.57$, the material behaves as brittle. When Poisson's ratio $\nu > 0.33$, the material exhibits plasticity and vice versa the material exhibits brittleness. As shown in Table 2 and Fig. 11, the B/G of all four NbMoTiZr-(Al/V) LRHEAs were greater than 1.57 and all of them are higher than that of the NbMoTaW-based refractory high entropy alloys [45,46]. It is shown that the room temperature plasticity of the four NbMoTiZr-(Al/V) LRHEAs were significantly improved compared to the NbMoTaW-based refractory high entropy alloys. All four NbMoTiZr-(Al/V) LRHEAs have $\nu > 0.33$ and $(C_{12}-C_{44}) > 0$, indicating that the four alloys have inherent intrinsic plasticity and metallic properties. On the other hand, as shown in Table 3, the B/G of the Zr_5Al_3 intermetallic compound is 1.92, which shows brittleness compared to the four alloys, indicating that the addition of the alloying element Al produces the Zr_5Al_3 intermetallic compound that makes the alloy brittle.

Hardness is defined as the combined resistance of the chemical bonds in the material to indentation, and it is closely related to the ductility of

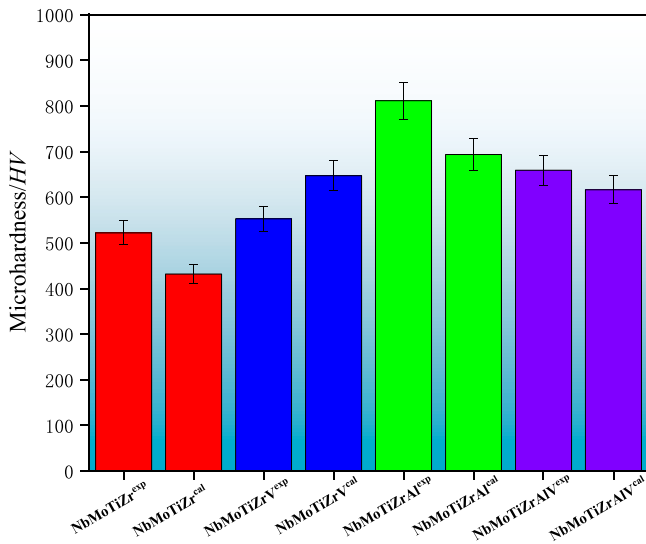


Fig. 12. Experimental and theoretical hardness of NbMoTiZr-(Al/V) LRHEAs.

the alloy. The theoretical hardness of the four LRHEAs were therefore calculated according to Eq. (18) proposed by Teter et al.[47].

$$H_V^{Teter} = 0.151G \quad (18)$$

where G is the calculated shear modulus, the experimental and theoretical hardnesses of the NbMoTiZr-(Al/V) LRHEAs were plotted in Fig. 12. The average hardness of the alloys measured in the tests were 521.86 HV, 552.74 HV, 811.29 HV and 659.01 HV. It can be seen that the addition of V and Al has improved the hardness of NbMoTiZr LRHEA and the theoretically calculated hardness of Zr₅Al₃ was 727.13 HV. Therefore the main reason for the significant increase in hardness with the addition of the alloying element Al is the formation of the Zr₅Al₃

intermetallic compounds. The predicted hardness values of the alloys are in good agreement with the experimental values, indicating that the first-principles calculation method adopted based on the density flood theory for predicting the hardness of high entropy alloys is feasible.

3.4. Electronic structure

Fig. 13 shows the energy band structure of each of the four NbMoTiZr-(Al/V) LRHEAs along the highly symmetric direction of the Brillouin zone. The red dashed line indicates the position of the Fermi energy level, and the energy band structure near the Fermi energy level is closely related to the properties of the material. As the conduction and valence bands overlap, the energy gap is zero, indicating that all four LRHEAs exhibit metallic properties[48]. Furthermore, compared to the NbMoTiZr LRHEA, the overlap of the energy bands increases significantly with the addition of V and Al, indicating stronger interatomic interactions and contributing to the improvement in mechanical properties.

Since the macroscopic mechanical properties of alloys are closely related to their electronic structure and atomic interactions. Therefore, the contribution of each element in the four LRHEAs to the total and partial densities of states (TDOS and PDOS) of the LRHEAs were calculated and plotted in Fig. 14. The black dashed line indicates the Fermi energy level. All four LRHEAs are electrically conductive and exhibit metallic properties due to the high density states of the Fermi energy levels[49]. The energies corresponding to the nearest double strong peaks on the Fermi energy level line are –0.18 eV and 2.92 eV for NbMoTiZr LRHEA, –0.33 eV and 2.39 eV for NbMoTiZrV LRHEA, –0.43 and 0.79 eV for NbMoTiZrAl LRHEA, and –0.34 eV and 0.91 eV for NbMoTiZrAlV LRHEA. The pseudo-energy gap is the capability difference between the two nearest strongest peaks near the Fermi energy level, reflecting the covalency of the alloy system; the wider the pseudo energy gap, the stronger the covalency[40]. The pseudo-energy gaps of the four LRHEAs are 3.1 eV, 2.72 eV, 1.22 eV, and 1.25 eV. Calculations show that the valence band of V and Al added to the alloy system is

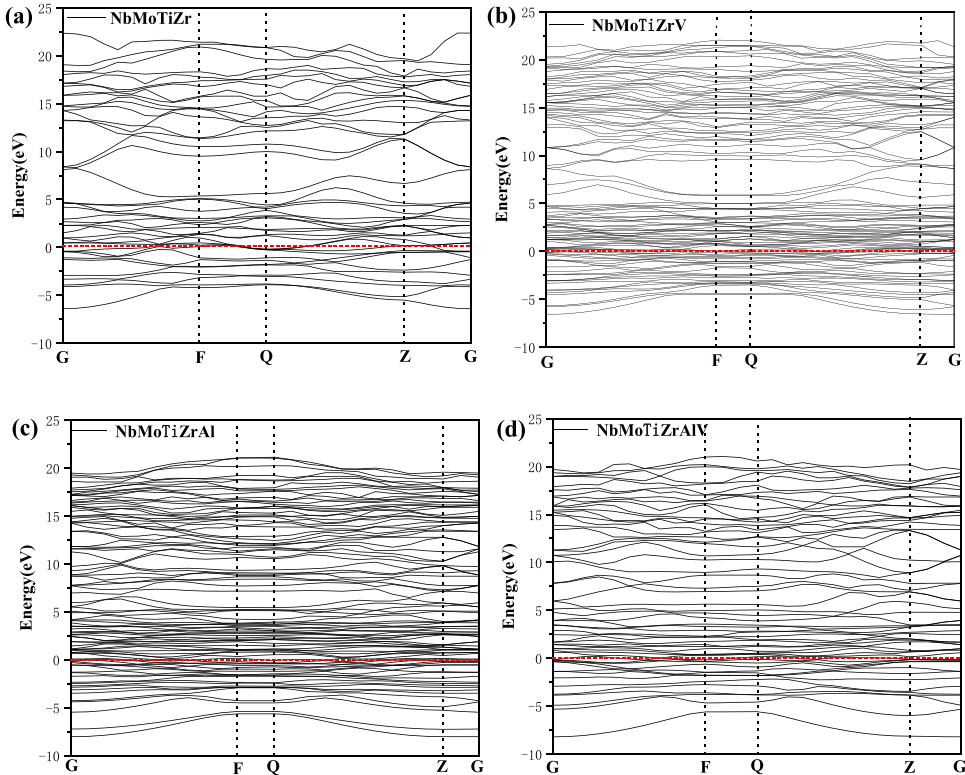


Fig. 13. Energy band structure of NbMoTiZr-(Al/V) LRHEAs (a) NbMoTiZr (b) NbMoTiZrV (c) NbMoTiZrAl (d) NbMoTiZrAlV.

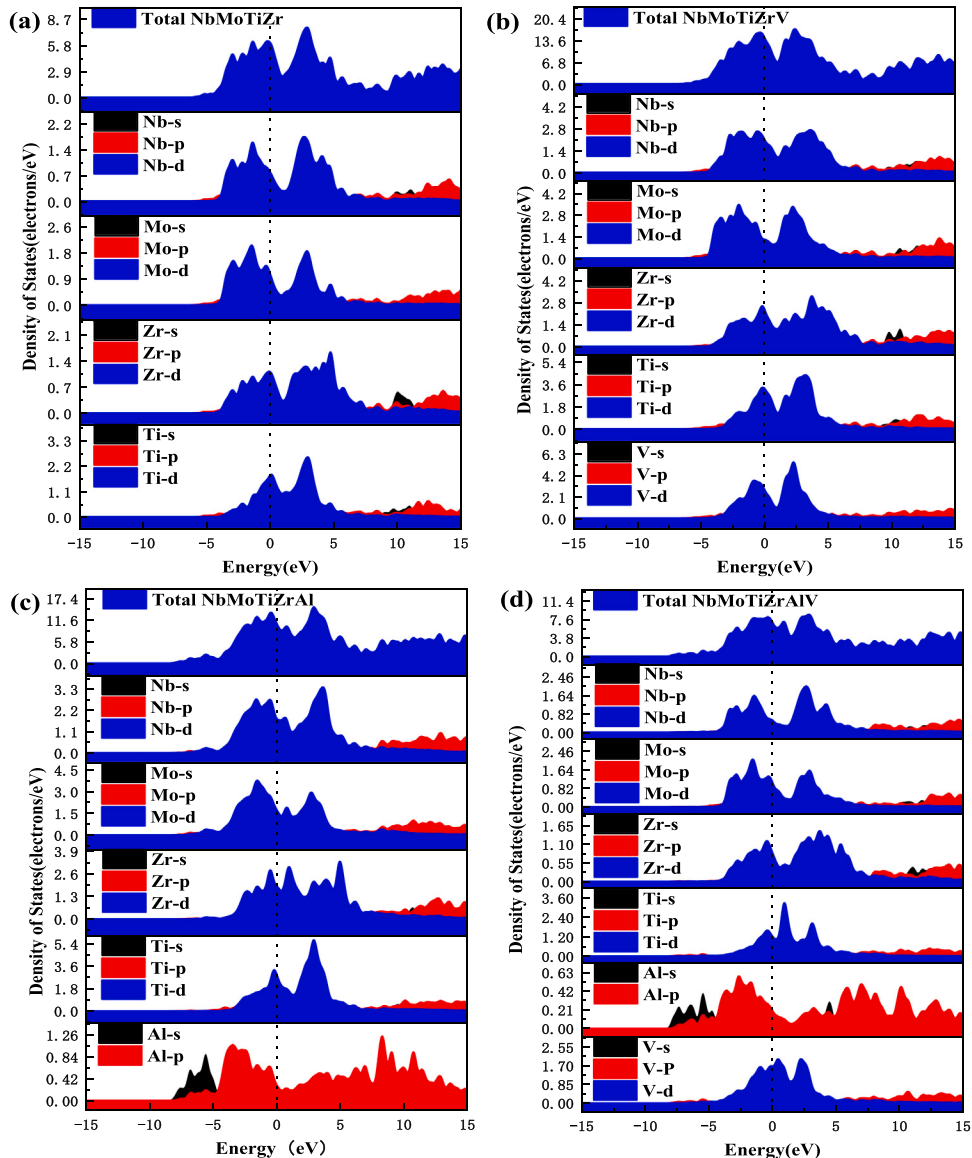


Fig. 14. Electron total and fractional density of states for NbMoTiZr-(Al/V) LRHEAs: (a) NbMoTiZr (b) NbMoTiZrV (c) NbMoTiZrAl (d) NbMoTiZrAlV.

significantly closer to the Fermi energy level and the conduction band is flatter. The reduction in covalency in the alloys increases metallic bonding, increased bond strength and improved mechanical properties. The analytical results are in good agreement with the Cauchy pressure bonding and energy bonding evaluations. In addition, the total density of states of the four NbMoTiZr-(Al/V) LRHEAs are much larger than that of the NbMoTaW RHEA, suggesting stronger metallic properties compared to the NbMoTaW RHEA.

From the PDOS of each alloy, it can be seen that there is a significant overlap in the state partial density of state curves of different atoms, indicating that there are strong electronic hybridization and covalent phenomena in the alloys. With the addition of alloying elements to the NbMoTiZr LRHEAs, the conduction bonds become more compact, indicating stronger orbital-electron interactions. The covalency of the NbMoTiZr-(Al/V) LRHEAs are mainly due to the hybridization of a large number of d-orbital electrons in the Nb, Mo, Ti, Zr, and V atoms, and p-orbital electrons in the Al atoms. In addition, the DOS at the Fermi energy level of the LRHEAs with added alloying elements is higher than that of the NbMoTiZr LRHEAs, suggesting that they improve the metal properties.

The plasticity/brittleness of a material is correlated with overlapping

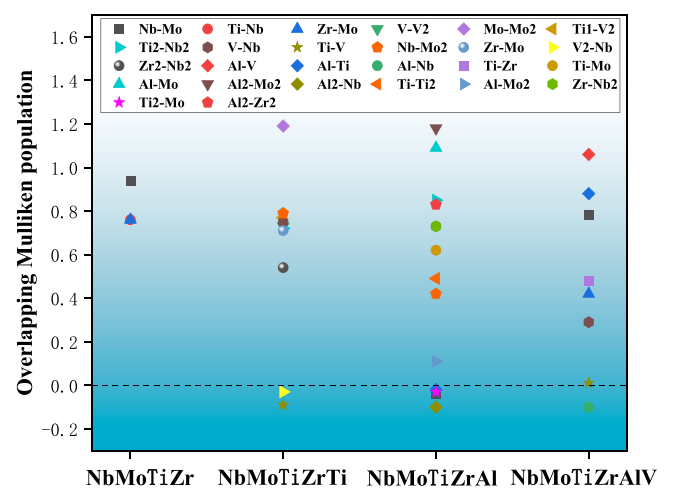


Fig. 15. Overlapping Mulliken population of NbMoTiZr-(Al/V) LRHEAs.

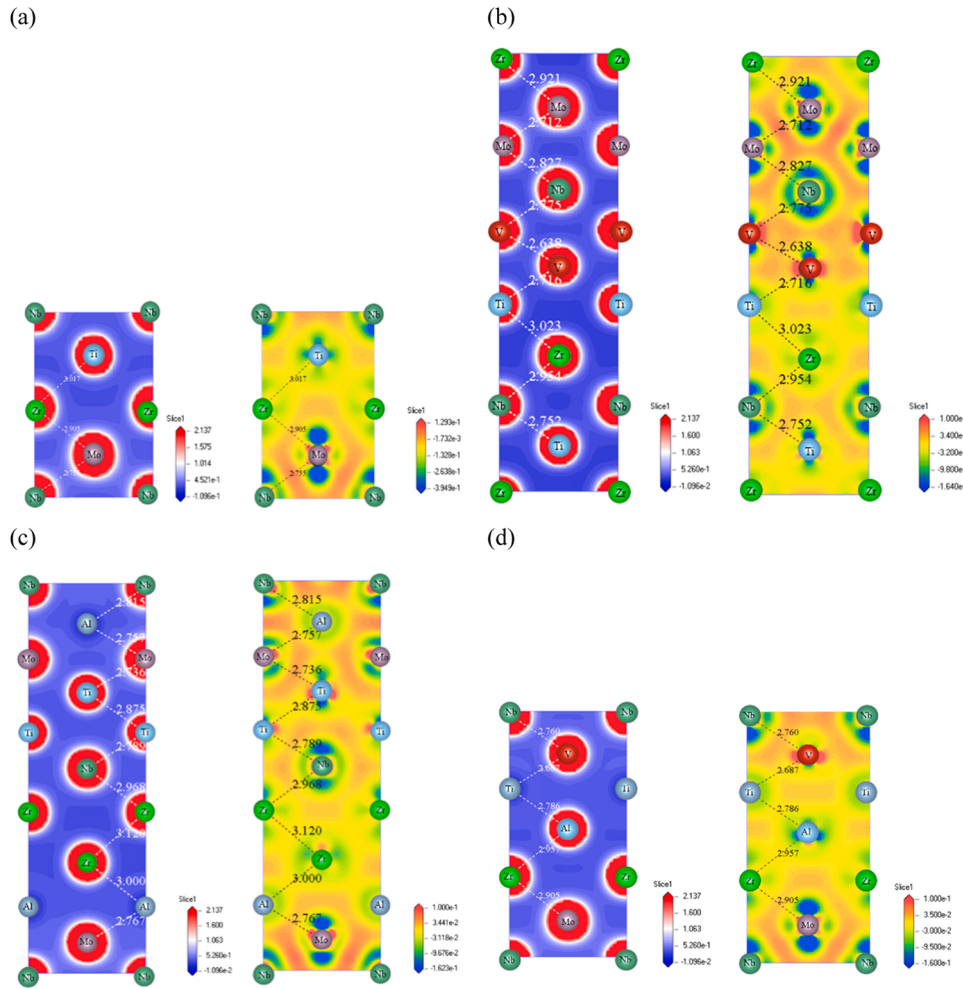


Fig. 16. Charge density diagram and charge density difference diagram of NbMoTiZr-(Al/V) LRHEAs: (a) NbMoTiZr (b) NbMoTiZrV (c) NbMoTiZrAl (d) NbMoTiZrAlV.

Mulliken populations. Generally, the positive value of the overlapping Mulliken population symbolizes the material combination of covalent bonds[50]. The larger the value, the stronger the covalent bonds and the less plastic the material. The negative value of overlapping Mulliken population indicates that anti-bonds will form in the alloy and the repulsive forces between atoms will increase[44]. The plasticity and brittleness of NbMoTiZr-(Al/V) LRHEAs can be indirectly determined by the degree of covalency and the type of bonding. As in Fig. 15, overlapping Mulliken population (P) as well as the bond lengths (\AA) of bonding atoms of NbMoTiZr-(Al/V) LRHEAs were systematically calculated. The NbMoTiZr LRHEA was only covalently bonded and, similar to NbMoTaW RHEA, showed brittle behavior with low strain in the room temperature stress-strain curve. Covalent bonding dominates in the LRHEAs with the addition of V and Al elements, while different types of chemical bonds are formed. The increase in the types of chemical bonds and the increasingly complex interatomic interactions result in systems that are less covalent and more metallic. In addition, overlapping Mulliken populations of V2-Nb, Ti-V, Nb-Mo, Al-Ti, Al2-Nb, Ti2-Mo and Al-Nb chemical bonds are all below zero. This means that these atoms are no longer covalently bonded and may be related to metallic bonding. Therefore, the results of the analysis of the overlapping Mulliken population indicate that the strength and ductility of these four NbMoTiZr-(Al/V) LRHEAs have been improved.

The charge density diagram reflects the degree of electron interaction between atoms and the type of bonding, and plays an important role in determining the plasticity and brittleness of materials. Fig. 16 shows

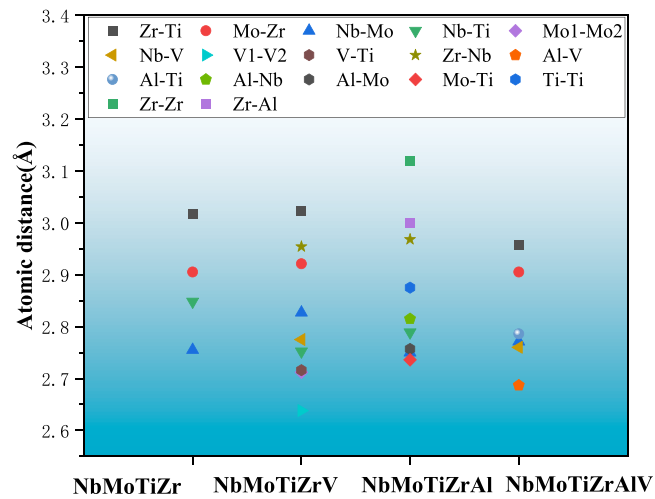


Fig. 17. Atomic distances of NbMoTiZr-(Al/V) LRHEAs.

the charge density and charge density difference plots of the four NbMoTiZr-(Al/V) LRHEAs along the grain surface (110). The charge density distribution around the atom is almost uniformly spherical, with the red color representing regions of higher charge density and the blue part representing regions of lower charge density. The large electron

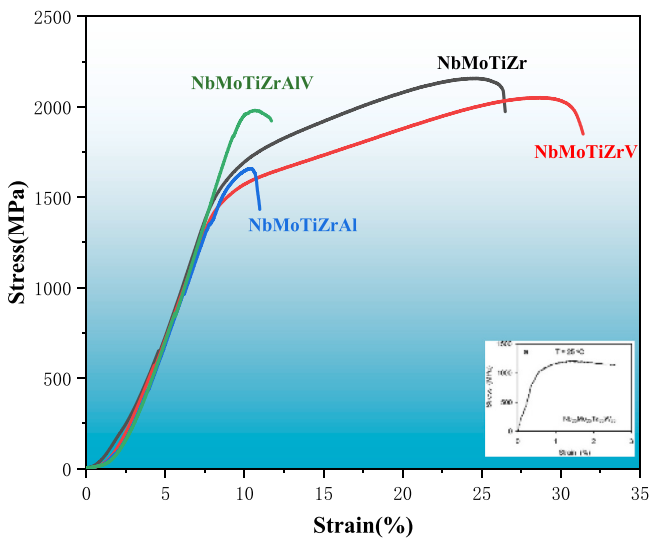


Fig. 18. The engineering compressive stress-strain curves of NbMoTiZr-(Al/V) LRHEAs.

Table 4
Compressive properties of NbMoTiZr-(Al/V) LRHEAs.

Alloys	Yield stress $\sigma_{0.2}$ (MPa)	Peak stress σ_b (MPa)	Peak strain ϵ_b (%)
NbMoTaW[11]	1058	1211	< 3
NbMoTiZr	1462	2158	24.6
NbMoTiZrV	1413	2051	28.7
NbMoTiZrAl	1527	1658	10.3
NbMoTiZrAlIV	1945	1980	10.6

enrichment in the vicinity of the metal atoms, the strong interactions between the electrons, and the apparent directionality indicate that covalent bonding plays a dominant role in the alloy system. It is noteworthy that for NbMoTiZrAl LRHEA and NbMoTiZrAlIV LRHEA the electron migration between Ti-Ti, Zr-Zr and Zr-Al were evident in the charge density difference diagrams, forming metallic bonds. As a result, the alloys with the addition of Al and V are less covalent and more metallic. This is consistent with the electronic density of states results above.

The atomic distances reflect the mechanical properties of the material. Fig. 17 shows the distances between the pairs of atoms in the equilibrium structure after relaxation. The atomic distances do not vary

much, except for the large difference in atomic pairs between Zr and other elements. This may be the reason for the good compressive mechanical properties of the four NbMoTiZr-(Al/V) LRHEAs, since the larger atomic radius of Zr compared to the other atoms gives the alloys lattice distortion and solid solution strengthening effects.

3.5. Mechanical properties

To further confirm the mechanical properties of the four NbMoTiZr-(Al/V) LRHEAs, engineered compressive stress-strain curves were prepared and measured at room temperature. As shown in Fig. 18 and Table 4. Compared to NbMoTaW RHEA [11], the results show a significant increase in the strength and plasticity of the alloy. The yield stress of NbMoTiZr-(Al/V) LRHEAs was increased by 33.5%–83.8%. NbMoTiZrAlIV LRHEA has the highest yield strength up to about 1945 MPa. The peak stresses have been increased by 36.9%–78.2%. The NbMoTiZr LRHEA had the highest peak stress of about 2158 MPa. The peak strains of NbMoZrTi and NbMoZrTiV LRHEAs reached about 24.6% and 28.7% respectively, which were much higher than the peak strains of NbMoTaW RHEA. The experimental data are in good agreement with the calculations of elastic constants and modulus of elasticity.

Fig. 19 shows the compression fracture morphology of NbMoTiZr-(Al/V) LRHEAs, the fracture morphology of the alloy did not find typical tough nests, the fractures are relatively flat, the fracture has many river-like patterns, which is a typical deconstructive fracture morphology, showing brittle fracture[51]. In particular, the presence of Zr₅Al₃ phase in NbMoTiZrAl and NbMoTiZrAlIV LRHEAs affect the properties of the alloys to some extent due to some brittleness, resulting in low ductility of the alloys.

4. Conclusion

In conclusion, in order to reduce the density and improve the mechanical properties of NbMoTaW RHEA. In this study, four novel lightweight refractory high entropy alloys were redesigned and prepared. The strengthening effect of the four alloys were investigated experimentally by combining the first-principle calculations. First-principle calculations were performed to compute the phase structure, lattice constant, density, elastic properties and electronic structure of NbMoTiZr-(Al/V) LRHEAs. Phase diagrams, first-principle calculations and empirical formulae indicate that all four NbMoTiZr-(Al/V) LRHEAs have stable BCC structures. The improvement of alloy properties by the addition of V/Al were further characterized by empirical equations for C₁₂-C₄₄, ν , B/G and HV. The energy bond structure, total density of states, partial densities of states, and charge densities show that the alloys have strong atomic interactions and metallic bonding of Ti-Ti, Zr-Zr,

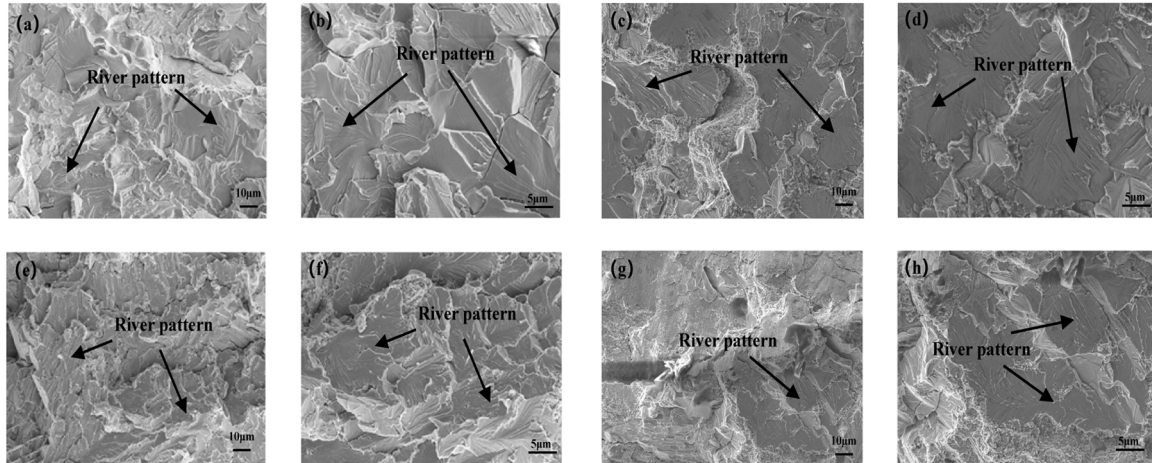


Fig. 19. SEM image of the fracture surfaces of (a, b) NbMoTiZr; (c, d) NbMoTiZrV; (e, f) NbMoTiZrAl; (g, h) NbMoTiZrAlIV LRHEAs after compression deformation.

and Zr-Al. The four alloys exhibit electrical conductivity and metallic properties.

To confirm the reliability of the first-principle calculations. The as-cast NbMoTiZr-(Al/V) LRHEAs were prepared and analyzed for microstructure and mechanical properties. The XRD data and microstructures demonstrate that the addition of the alloying element Al results in the presence of the B2 phase and the Zr₅Al₃ phase, except for the NbMoTiZr and NbMoTiZrV alloys, which have a single BCC solid solution structure. All four NbMoTiZr-(Al/V) LRHEAs are stronger and more ductile than NbMoTaW RHEA, with NbMoTiZr LRHEA having greater strength and NbMoTiZrV LRHEA having greater ductility. These results are in good agreement with the calculated results. Compared to NbMoTaW RHEA, this alloy system is effective in improving the mechanical properties and further reducing the alloy density. To examine alloy strengthening of LRHEAs and other alloys. The present work demonstrates that first-principle calculations are a viable tool for predicting the properties of LRHEA.

CRediT authorship contribution statement

Wenjie Chen: Investigation, Methodology, Data curation, Writing – review & editing. **Xinmei Li:** Funding acquisition, Supervision, Project administration, Investigation.

Declaration of Competing Interest

The authors declare that they have no known competing financial interests or personal relationships that could have appeared to influence the work reported in this paper.

Data Availability

Data will be made available on request.

Acknowledgments

The work was supported by National Natural Science Foundation of China (No. 52161017) and Natural Science Foundation of Xinjiang Uygur Autonomous Region (2022D01C386).

References

- [1] Barnasree Chanda, Jayanta Das, An assessment of the stability of the eutectic phases in high entropy alloys, *J. Alloy. Compd.* 798 (2019) 167–173.
- [2] J.W. Yeh, S.Y. Chang, Y.D. Hong, et al., Anomalous decrease in X-ray diffraction intensities of Cu–Ni–Al–Co–Cr–Fe–Si alloy systems with multi-principal elements, *Mater. Chem. Phys.* 103 (2007) 41–46.
- [3] K.Y. Tsai, M.H. Tsai, Yeh, J.W. Yeh, Sluggish diffusion in Co-Cr-Fe-Mn-Ni high-entropy alloys, *Acta Mater.* 61 (2013) 4887–4897.
- [4] RajivS. Mishra, Haridas Ravi Sankar, Priyanshi Agrawal, High entropy alloys – Tunability of deformation mechanisms through integration of compositional and microstructural domains, *Mat. Sci. Eng. A-Struct.* 812 (2021).
- [5] Chungjin Tong, Yuliang Chen, Jianwei Yeh, et al., Microstructure characterization of Al_xCoCrCuFeNi high-entropy alloy system with multiprincipal elements, *Metall. Mater. Trans. A*. 36 (2005) 881–893.
- [6] O.N. Senkov, J.M. Scott, S.V. Senkova, et al., Microstructure and room temperature properties of a high-entropy TaNbHfZrTi alloy, *J. Alloy. Compd.* 509 (2011) 6043–6048.
- [7] Takeuchi, Akira Amiya, et al., High-entropy alloys with a hexagonal close-packed structure designed by equi-atomic alloy strategy and binary phase diagrams, *JOM* 66 (2014) 1984–1992.
- [8] L. Lilenstein, J.P. Couzinié, L. Perrière, et al., New structure in refractory high-entropy alloys, *Mater. Lett.* 132 (2014) 123–125.
- [9] L.J. Zhang, P.F. Yu, M.D. Zhang, et al., Microstructure and mechanical behaviors of Gd x CoCrCuFeNi high-entropy alloys, *Mat. Sci. Eng. A-Struct.* 707 (2017) 708–716.
- [10] O.N. Senkov, G.B. Wilks, D.B. Miracle, et al., LiawRefractory high-entropy alloys, *Intermetallics* 18 (2010) 1758–1765.
- [11] O.N. Senkov, G.B. Wilks, J.M. Scott, et al., Mechanical properties of Nb₂₅Mo₂₅Ta₂₅W₂₅ and V₂₀Nb₂₀Mo₂₀Ta₂₀W₂₀ refractory high entropy alloys, *Intermetallics* 19 (2011) 698–706.
- [12] G.B. Chen, Y. Xiao, X.X. Ji, et al., Effects of Zr Content on the Microstructure and Performance of TiMoNbZrx High-Entropy Alloys, *Metals* 11 (2021) 1315.
- [13] Qian Zhi, Xinrong Tan, Zhongxia Liu, et al., Effect of Zr content on microstructure and mechanical properties of lightweight Al₂NbTi3V2Zrx high entropy alloy, *Micron* 144 (2021).
- [14] T.T. Zuo, R.B. Li, X.J. Ren, et al., Effects of Al and Si addition on the structure and properties of CoFeNi equal atomic ratio alloy, *J. Magn. Magn. Mater.* 371 (2014).
- [15] C. Li, J.C. Li, M. Zhao, et al., Effect of aluminum contents on microstructure and properties of Al_xCoCrFeNi alloys, *J. Alloy. Compd.* 504 (2010).
- [16] C.M. Lin, C.C. Juan, C.H. Chang, et al., Effect of Al addition on mechanical properties and microstructure of refractory Al_xHfNbTaTiZr alloys, *J. Alloy. Compd.* 624 (2015).
- [17] Y.H. Chen, W.K. Liu, H.W. Wang, et al., Effect of Ti Content on the Microstructure and Properties of CoCrFeNiMnTix High Entropy Alloy, *Entropy* 24 (2022) 241.
- [18] Td Huang, Sy Wu, H. Jiang, et al., Effect of Ti content on microstructure and properties of Ti_xZrVNb refractory high-entropy alloys, *Int. J. Miner. Metall. Mater.* 27 (2020) 1318–1325.
- [19] N.Yu Yurchenko, N.D. Stepanov, S.V. Zhrebtssov, et al., Structure and mechanical properties of B2 ordered refractory AlNbTiVZrx ($x = 0\text{--}1.5$) high-entropy alloys, *Mat. Sci. Eng. A-Struct.* 704 (2017).
- [20] Vipul Bhardwaj, Qing Zhou, Fan Zhang, et al., Effect of Al addition on the microstructure, mechanical and wear properties of Ti_xZrNbHf refractory high-entropy alloys, *Tribol. Int.* 160 (2021).
- [21] Z.D. Han, N. Chen, S.F. Zhao, et al., Effect of Ti additions on mechanical properties of NbMoTaW and VNbMoTaW refractory high entropy alloys, *Intermetallics* 84 (2017).
- [22] G.A. Salishchev, M.A. Tikhonovsky, D.G. Shaysultanov, et al., Effect of Mn and V on structure and mechanical properties of high-entropy alloys based on CoCrFeNi system, *J. Alloy. Compd.* 591 (2014).
- [23] P. Zhao, J. Li, Y. Zhang, et al., Wear and high-temperature oxidation resistances of AlNbTaZrx high-entropy alloys coatings fabricated on Ti6Al4V by laser cladding, *J. Alloy. Compd.* 862 (2021).
- [24] S.Y. Chen, X. Yang, K.A. Dahmen, et al., Microstructures and Crackling Noise of AlNbTiMoV High Entropy Alloys, *Entropy* 16 (2014) 870–884.
- [25] Stewart J. Clark, Matthew D. Segall, Chris J. Pickard, et al., First Princ. Methods Using CASTEP, *Z. Krist.* (220) () (2009).
- [26] Alex Zunger, S.H. Wei, L.G. Ferreira, et al., Special quasirandom structures, *Phys. Rev. Lett.* 65 (1990) 353.
- [27] A. van de Walle, P. Tiwary, M. de Jong, et al., Efficient stochastic generation of special quasirandom structures, *Calphad* 42 (2013) 13–18.
- [28] J.P. Perdew, K. Burke, Y. Wang, Generalized gradient approximation for the exchange-correlation hole of a many-electron system, *Phys. Rev. B* 77 (1996) 48–53.
- [29] Matthias Ernzerhof, Gustavo E. Scuseria, Assessment of the Perdew–Burke–Ernzerhof exchange-correlation functional, *J. Chem. Phys.* 110 (1999) 5029–5036.
- [30] G. Kresse, J. Hafner, Norm-conserving and ultrasoft pseudopotentials for first-row and transition elements, *J. Phys. Condens. Mat.* 6 (1994).
- [31] M.D. Feit, J.A. Fleck, A. Steiger, Solution of the Schrödinger equation by a spectral method, *J. Comput. Phys.* 47 (1982) 412–433.
- [32] Fuen Zhang, Baifeng Luan, Linhua Chu, et al., Effects of composition on phase stabilities and elastic properties in Ti_xZrAlV alloys: Experiments and first-principles calculations, *J. Alloy. Compd.* 863 (2021).
- [33] Shiquan Feng, Yang Yang, Feng Guo, et al., Structural, elastic, electronic and hardness properties of osmium diboride predicted from first principles calculations, *J. Alloy. Compd.* 844 (2020).
- [34] Jing Feng, Bing Xiao, Rong Zhou, et al., Anisotropic elastic and thermal properties of the double perovskite slab-rock salt layer Ln₂ SrAl₂O₇ (Ln=La, Nd, Sm, Eu, Gd or Dy) natural superlattice structure, *Acta Mater.* 60 (2012) 3380–3392.
- [35] Y.J. Sun, K. Xiong, S.M. Zhang, et al., First-principles investigations on the elastic properties of platinum group metals (Pt, Pd, and Ru), *MSF* 944 (2019) 761–769.
- [36] Yong Zhang, Ting Ting Zuo, Zhi Tang, et al., Microstructures and properties of high-entropy alloys, *Prog. Mater. Sci.* 61 (2014) 1–93.
- [37] Wei Li, Ping Liu, Peter K. Liaw, Microstructures and properties of high-entropy alloy films and coatings: a review, *Mater. Res. Lett.* 6 (2018) 199–229.
- [38] S.P. Wang, Evan Ma, Jian Xu, New ternary equi-atomic refractory medium-entropy alloys with tensile ductility: hafnium versus titanium into NbTa-based solution, *Intermetallics* 107 (2019) 15–23.
- [39] H.W. Yao, J.W. Qiao, J.A. Hawk, et al., Mechanical properties of refractory high-entropy alloys: experiments and modeling, *J. Alloy. Compd.* 696 (2017) 1139–1150.
- [40] Y.L. Hu, L.H. Bai, Y.G. Tong, et al., First-principle calculation investigation of NbMoTaW-based refractory high entropy alloys, *J. Alloy. Compd.* 827 (2020).
- [41] Z.S. Nong, J.C. Zhu, R.D. Zhao, Prediction of structure and elastic properties of AlCrFeNiTi system high entropy alloys, *Intermetallics* 86 (2017).
- [42] M.L. Huang, C.Y. Wang, First-principles studies of effects of interstitial boron and carbon on the structural, elastic, and electronic properties of Ni solution and Ni₃Al intermetallics, *Chin. Phys. B* 25 (2016).
- [43] W. Chen, Q.H. Tang, H. Wang, et al., Microstructure and mechanical properties of a novel refractory AlNbTiZr high-entropy alloy, *Mater. Sci. Technol. -Lond.* 34 (2018) 1309–1315.
- [44] M.C. Gao, Y. Suzuki, H. Schweiger, et al., Phase stability and elastic properties of Cr-V alloys, *J. Phys. Condens. Mat.* 25 (2013).
- [45] Yonggang Tong, Linhui Bai, Xiubing Liang, et al., Influence of alloying elements on mechanical and electronic properties of NbMoTaWX (X = Cr, Zr, V, Hf and Re) refractory high entropy alloys, *Intermetallics* 126 (2020).

- [46] Linhui Bai, Yongle Hu, Xiubing Liang, et al., Titanium alloying enhancement of mechanical properties of NbTaMoW refractory high-Entropy alloy: First-principles and experiments perspective, *J. Alloy. Compd.* 857 (2021).
- [47] M. David Teter, Computational alchemy: the search for new superhard materials, *MRS Bull.* 23 (1998) 22–27.
- [48] Zhenhua Yang, Li Liu, Xianyou Wang, et al., Stability and electronic structure of the Co–P compounds from first-principle calculations, *J. Alloy. Compd.* 509 (2010) 165–171.
- [49] Jian Zhang, Qi Xu, Yongle Hu, et al., Interfacial bonding mechanism and adhesive transfer of brazed diamond with Ni-based filler alloy: First-principles and experimental perspective, *Carbon* 153 (2019) 104–115.
- [50] Yijie Wang, Yazhou Xue, Mao Pan, et al., Interaction of salicylhydroxamic acid with the surface of MgTi₂O₅: a study combined DFT and experiment, *J. Alloy. Compd.* 774 (2019) 222–228.
- [51] I. Konovalenko, P. Maruschak, J. Brezinová, et al., Morphological characteristics of dimples of ductile fracture of vt23m titanium alloy and identification of dimples on fractograms of different scale, *Materials* 12 (2019) 2051.